

# Advanced Ultrasonic Imaging Techniques for Breast Cancer Research <sup>1</sup>

Michael Insana <sup>a,2</sup> and Michael Oelze <sup>b</sup>

<sup>a</sup> *Depts. of Bioengineering and ECE, University of Illinois*

<sup>b</sup> *Dept. of Electrical and Computer Eng., University of Illinois*

**Keywords.** elasticity imaging, histology, microenvironment, scatterer size imaging, viscoelasticity

## 1. Introduction

The goal of cancer imaging is to exploit disease-specific object contrast mechanisms that provide very specific information about cellular structure and function to help diagnose and manage diseases and to develop tools for scientific investigation. This chapter reviews several ultrasonic methods for obtaining detailed histological descriptions of mammary tissue noninvasively that are related directly to tumor growth.

Ultrasonic imaging (sonography) is now routinely applied in a clinical setting as an adjunct to mammography and the physical examination. Its role is primarily to differentiate solid tumors from cysts and to guide needle and surgical excision biopsies. Tumors larger than 8 mm are readily detected as hypoechoic (lower echo strength) regions. Unfortunately sonographic features are frequency nonspecific; the appearance of benign masses, such as fibrocystic lesions and fibroadenomas, is often similar to that of malignant lesions, such as infiltrating ductal carcinoma (IDC) and infiltrating lobular carcinoma (ILC). Sonography is very useful for locating lesions and ruling out cysts, although the definitive differential diagnosis requires pathological analysis of biopsy samples. A needle biopsy is minimally invasive but suffers from sampling errors; small lesions can be easily missed. Surgical biopsies remove more tissue, reducing sampling errors, but introduce the risks and expenses associated with any surgical procedure. Surgical biopsy is a hybrid diagnostic-therapeutic procedure, so we would like to use it only when we're reasonably confident that cancer is present. Our goal is to increase the diagnostic information provided by ultrasound scans safely and at low cost, so that frequent serial imaging of patients at risk can be applied to reduce the number of questionable biopsies without sacrificing diagnostic performance. Such methods can be used periodically for the initial diagnosis and regularly for monitoring a patient's response to treatment.

---

<sup>1</sup>This work was supported in part by NIH R01 CA082497.

<sup>2</sup>Correspondence to: Michael Insana, Department of Bioengineering, University of Illinois at Urbana-Champaign, 1304 Springfield Ave., MC-278, Urbana, IL 61801. Tel.: +1 217 244 0739; Fax: +1 217 265 0246; E-mail: mfi@uiuc.edu.

Working against our proposed expanded use of ultrasound is the complexity and diversity of breast cancer and natural inter-patient variability. Since histopathology is how cancer is defined, it is completely accurate at one instant of time except for human error. Radiological procedures are strong at detecting and localizing lesions but are rarely used to classify disease since images only describe a small subset of the total histological feature space. Thus it is unlikely that any one diagnostic test can reliably detect and classify breast cancers in all patients.

Identifying diverse disease processes is improved by increasing the feature space for classification. The best strategy is to provide decision makers with several independent features related uniquely to tissue properties that span the range of disease phenotypes. A simple example is the current combination of mammography and palpation. Mammography is most accurate for detecting early tumors that produce microcalcifications. Manual palpation exposes tumors that become mechanically stiff. Insofar as the effects are uncorrelated, their combination more effectively aids diagnosis than each applied individually. Even recent molecular imaging methods that seek to reveal and treat suspicious regions based on high angiogenic activity can fail when used alone [45]. Promising new approaches strive to recognize tumors that express a broad range of angiogenic factors and related molecular signals. Like other researchers, we have turned to the molecular biology of cancer to find hallmark features for imaging.

From the literature of the past two decades, a richly detailed picture of the biology of breast cancer is emerging [16, 61, 78]. It is clear that the initiation, rate of progression, and occurrence of malignant transformation are determined by a combination of genetic and epigenetic factors; the later encompassed by the term “cellular microenvironment”. Many of these discoveries suggest new opportunities for combined cancer imaging and treatment that promise increased sensitivity and specificity. One manifestation is the new field of molecular imaging [4, 60, 79]. Most molecular imaging approaches include development of blood-borne particles, known as probes or beacons, with biologically active surfaces. These particles target disease-specific molecular sites in the body and emit or reflect energy that can be sensed by current imaging modalities [1, 13, 50]. The development of targeted contrast agents is largely a chemical synthesis problem; one of being able to functionalize particle surfaces so they remain stably active while circulating in the blood stream seeking their targets.

Our approach is to image histological features of breast tissues that influence the cellular microenvironment (defined below) without contrast enhancement through the unique capabilities of ultrasound. Ultrasound is highly sensitive to subtle variations in the mechanical properties of tissues at many scales that often change as the composition and distribution of cells is modified by disease. To model sound tissue interactions, tissues are viewed from the materials science viewpoint as a viscoelastic continuum (think of gelatin) in which compressional sound waves travel. Within glandular tissues, cells, connective tissues and the microvasculature reflect a small amount of the sound energy back to the detector. Because the wavelength of diagnostic ultrasound ( $150\ \mu\text{m}$ ) is about 300 times longer than the wavelength of visible light (500 nm), the spatial resolution possible for ultrasound is far below optical microscopy. Nevertheless, lower attenuation allows ultrasound to penetrate deeper into the body than light and therefore it is unnecessary to extract tissue samples for analysis. Rather than resolving individual structures, a statistical ultrasonic analysis examines the statistical properties of echo signals to estimate average properties of tissue structures at the scale of the cell. For example, we

can create parametric ultrasound images where the image pixels represent the average size of scatterers. Using pre-image echo signals from clinical instruments and advanced signal processing methods, parametric ultrasound images quantify structural features of fibrotic tissues and regions of cellular hypertrophy and hyperplasia with the spatial resolution of sonography. In this application, ultrasound is applied to describe *microscopic mechanical properties* of tissues.

We can also use ultrasound to track tissue motion and thereby observe the *macroscopic mechanical properties* of tissues using the techniques of elasticity imaging. As we show below, cancer modifies how cells are connected to one another over a long distance, a feature of the disease that is often missed by histopathology. Ultrasound can detect the spatial distribution of tiny local movements caused when tissues are gently squeezed to estimate viscoelastic properties with the spatial resolution of sonography. Elasticity imaging can describe desmoplasia, edema, and other processes that stiffen tissue. It also describes ultrastructural changes to the intra- and inter-lobular stroma that alter how water is attracted to the extracellular matrix and how collagen fibers are cross linked. Combining the microscopic and macroscopic ultrasonic features, we gain new perspectives on cancer progression and can track the course of disease safely and with low cost.

To be successful at this research requires a truly interdisciplinary effort, where the rapid advances in cancer biology are integrated with a precise understanding of how ultrasound interacts with tissues to view these processes. Consequently, our chapter begins with a review of modern theories of breast cancer formation and the interactions between ultrasonic energy and biological tissues.

## 2. Breast Cancer Biology

Molecular signaling between epithelial cells and its supporting stroma is essential for normal breast development and cyclic maintenance as well as tumorigenesis [16]. The most common cancers are carcinomas of the mammary duct and lobule (Fig 1) often beginning with mutations to the luminal epithelial cells. Growth promoting proteins stimulate the oncogenic mutations to proliferate not into homogeneous masses of epithelial cells but into heterogeneous, mixed-cell-type tumors containing epithelial, fibroblast, smooth muscle, and inflammatory cells (Fig 2). Genetic alterations to epithelial cells alone cannot explain the diversity of tumor cell phenotypes nor the complexity of disease progression. There is now ample evidence to support the theory that epigenetic processes driven by microenvironmental factors play major roles in the development of breast cancers [26, 61].

The regional environment changes as cell types mix when the basement membrane (BM) separating epithelial cells from stroma degrades. The BM is a layer of extracellular collagen to which signaling molecules are attached. These molecules both direct and stabilize cell differentiation, polarization and overall 3-D organization [72]. The BM also serves as a barrier and conduit for various signaling molecules produced by the epithelium and stroma. The organization of cells in normal tissues is a balance between the tendency of the epithelium to stabilize morphometry by producing BM and the stroma that induces structural changes by selectively eroding the BM [61]. Stroma include fibroblasts, smooth muscle cells, nerve cells, and the extracellular matrix (ECM). In addition to the BM, mammary gland ECM includes the extracellular collagen-fiber network embed-

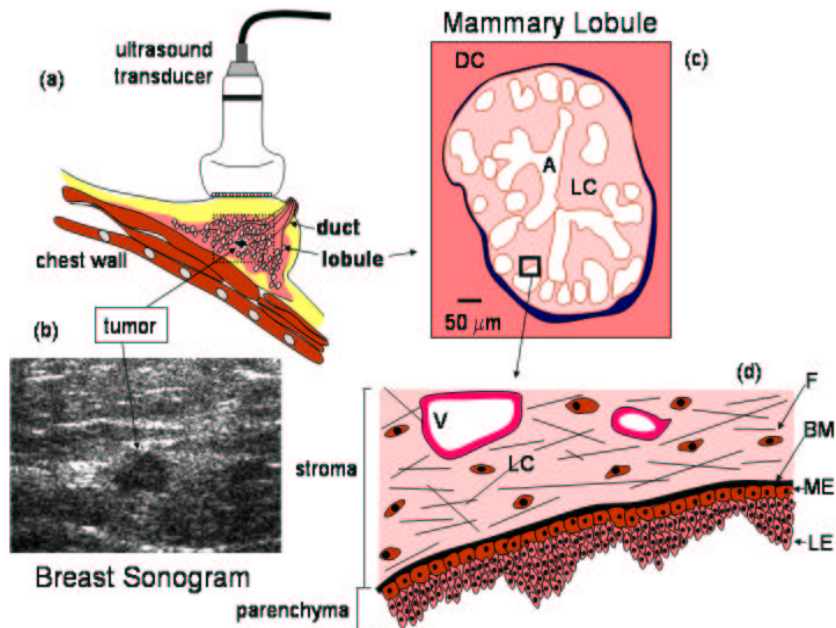


**Figure 1.** The gross and micro-anatomy of breast tissue. The breast is scanned ultrasonically (a) to generate a sonogram (b). Normal mammary lobule (c) composed of acini A in loose connective tissue stroma LC. Surrounding the lobules and ducts is the dense connective tissue DC of the interlobular space. Magnification of the acinus wall (d) shows basement membrane B separating LC stroma containing fibroblasts F and blood vessels V from the parenchymal tissues including a thin layer of myoepithelial cells ME and the luminal epithelium LE.

ded in “ground substance” that provides mechanical support. The ground substance is mostly long proteoglycan molecules that are hydrated glycoproteins covalently bonded to polysaccharide chains called glycosaminoglycans [38]. Also included are adhesive glycoproteins: two important examples are *fibronectin* that links cells to the ECM and *integrins* to facilitate cell movement within the ECM, and *laminin* that connects parenchymal cells to the ECM via the BM [11, 38, 70]. The stroma guides cell movement, organization and stability. Although wide-spread breakdown of BM is a histological indicator for malignant conversion, the loss of BM regulation of epithelial-stromal interactions also initiates neoplastic transformations [26]. Direct physical contact between glandular epithelial cells and the surrounding connective tissues promotes neovascularization, inflammation, and a major structural remodeling of the ECM (Fig 2). Ultrasonic methods enable us to observe the effects of this remodeling process, noninvasively, even if we cannot resolve cells directly.

Stromal remodeling follows the formation of myofibroblasts from normal stromal fibroblasts [63] or, as some suggest, from luminal-epithelial and myoepithelial cell conversions to myofibroblasts [58]. Myofibroblasts promote cancerous epithelial proliferation and generate large amounts of ECM collagen, smooth muscle actin and myosin, and growth factors that transform the quiescent connective tissues into reactive desmoplasia [16, 76] (Fig 2). Smooth muscle cells in the fibrous form of desmoplasia that surrounds many tumors will contract and stiffen lesions between one and two orders of

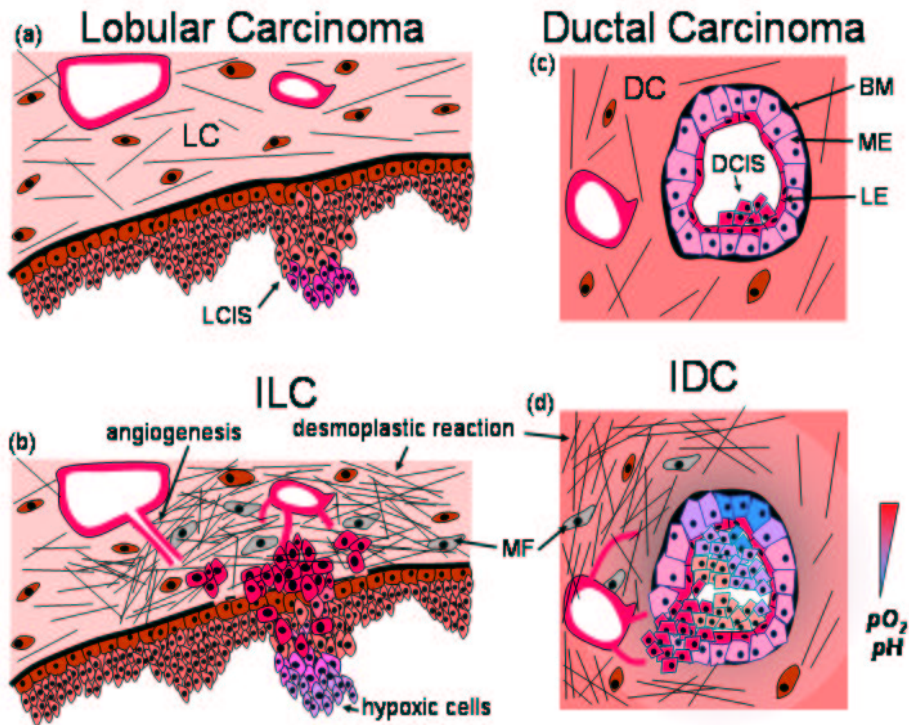


**Figure 2.** Illustration of the progression of lobular (a,b) and ductal (c,d) carcinomas from in situ disease (a,c) to invasive disease (b,d). Epithelial cell color indicates variations in pH and pO<sub>2</sub> levels. Myofibroblasts MF, lobular carcinoma in situ LCIS, ductal carcinoma in situ DCIS.

magnitude more than the surrounding tissue [33]. Thus many cancers can be palpated. Despite an increase in collagen that scatters ultrasound, tissues also become edematous from the collapse of lymph vessels. The combination (not fully understood) usually gives breast tumors the hypoechoic sonographic appearance shown in Fig 1(b).

Ligands and receptors, growth factors, proteases and their inhibitors all orchestrate complex signaling patterns between the epithelium and stroma to prepare the surrounding connective tissues for neovascularization as required for continuous tumor growth [6]. This process dynamically erodes and builds ECM in spatial patterns that direct the growth and stabilization of nascent vasculature. Knowledge of the mechanisms of tumor angiogenesis is maturing [32].

The rate of all this activity is regulated by the quickly evolving cellular microenvironment, which includes functional cell phenotype and spatial organization, cell adhesion sites, growth factors and metabolic activity. Tumors are heterogeneous mixtures of reactive cells. They become a dynamic and interactive functional unit capable of regulating tissue specific gene expression in the mammary gland [25]. The progression of breast cancer from in situ hyperplasia to metastatic disease involves interplay among cellular genetics and microenvironmental factors; the former can be monitored using molecular imaging and the later using the ultrasonic methods described below.

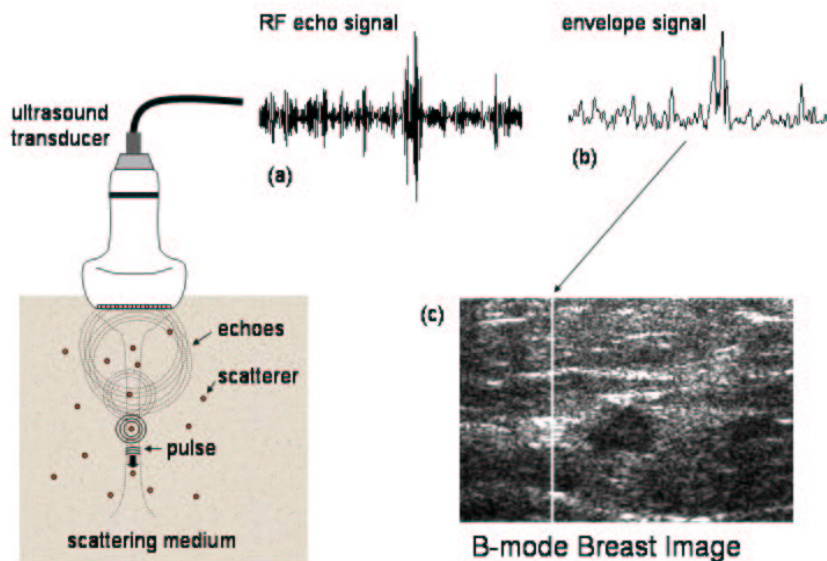


**Figure 3.** Illustration of ultrasonic echo generation and image formation. A broadband pulse transmitted by the transducer array is scattered as it propagates into the body along the beam axis. Immediately after transmitting, the array begins “listening” for backscattered echoes. Echo signals from individual array elements are combined to form the beamformed RF signal (a) used in our analyses. However sonograms are collections of adjacent RF signals that have been envelope detected (b), and whose amplitudes are logarithmically compressed and assigned gray-scale values before being placed (scan converted) in the image (c).

### 3. Opportunities for Ultrasonic Imaging

To describe how ultrasonic methods can help classify breast lesions we briefly summarize the physics of sound-tissue interactions [80]. Pulse-echo ultrasound relies on reflections (scattering) from tissue structures to produce the signal that appears in sonograms (Fig 3). Ultrasound waves are scattered at the surfaces of structures that vary in density and bulk compressibility [28]. The echo signal is most descriptive of the scatterer when the wavelength of sound is approximately equal to the size of the scatterer [27]; shorter wavelengths are absorbed more readily while longer wavelengths scatter less energy. In soft tissues at diagnostic imaging frequencies ( $<20$  MHz), the strongest scatterers are composed of mesenchymal cells. Specifically in breast tissues, scatterers include arterioles, mammary ducts and lobules – any connective tissue structure rich in collagen and elastin fibers and muscle cells [18] of size approximately equal to the wavelength. At higher frequencies, say 100 MHz, the wavelength of sound ( $15 \mu\text{m}$ ) can be just one to three times the size of the cell nucleus, and therefore epithelial cell structures contribute prominently to the echo signal [64]. The frequency of sound determines the scale of structures that scatter sound energy and to what degree. Identifying sources of ultrasonic scattering in biological media remains a topic of active investigation [29,43].

The wavelength also determines the limit of spatial resolution. Diffraction limited resolution for ultrasound is proportional to the wavelength of sound. The average speed

of a compressional sound wave in tissue is approximately 1540 m/s. At 10 MHz, the wavelength  $\lambda = 1.54 \text{ mm } \mu\text{s}^{-1}/10 \text{ MHz} \sim 0.15 \text{ mm}$ . For a Gaussian shape pulse and a transducer bandwidth of 50%, the axial resolution is approximately twice the wavelength, 0.3 mm. Similarly, a focused  $f/\# = 2.0$  transducer aperture provides a lateral resolution equal to the axial resolution,  $\lambda \times f/\# = 0.3 \text{ mm}$ .

Above 100 MHz, many mammary cells are resolvable. However the sound-wave energy is attenuated more at higher frequencies, reducing the scattered energy by  $\sim 100 \text{ dB}$  for every centimeter of tissue depth:  $0.5 \text{ dB cm}^{-1}\text{MHz}^{-1} \times 100 \text{ MHz} \times 2$  (to account for the two-way pulse-echo path.) The very high frequency range is the realm of acoustic microscopy [5] that parallels many of the advantages and limitations of optical microscopy.

When there is an average of 10 or more small scatterers per acoustic pulse volume that are randomly positioned, the statistical properties of the echo signal reveal the statistical properties of the tissue [73]. This is the full-developed speckle condition also responsible for the characteristic texture (speckle) of sonograms, e.g., see Fig 1(b). For randomly positioned  $30 \mu\text{m}$  scatterers, a pulse length larger than 0.3 mm generates fully-developed speckle and therefore the echo statistics are descriptive of the tissue structure. Consequently, a 10 MHz broadband pulse with 50% fractional bandwidth can directly image (resolve) structures  $300 \mu\text{m}$  and larger. However, by analyzing statistical moments of the echo signal, we can describe average properties of random scatterers of size near  $30 \mu\text{m}$  with the same 10 MHz pulse. The statistical analysis is less sensitive to scatterers much smaller than the wavelength, and requires more detailed information about scatterer shape and material properties to accurately describe larger structures.

### 3.1. Scatterer size imaging

Modeling tissues as a viscous fluid containing randomly positioned scattering sites, we adopt a statistical description of the cellular-scale structures [73]. Statistical moments of the RF echo signal (Fig 3) and its power spectrum (described in Section 5) can be used to estimate the average size and number density of scatterers contributing to the signal if we are allowed to make a few assumptions about the medium and the acoustic field geometry [8, 27, 36, 53]. Provided that the average properties of the scattering structure vary slowly with position, size and number density can be accurately estimated with a spatial resolution of  $1\text{-}5 \text{ mm}^3$ , and thus we form parametric images of mammary tumors [54]. Changing the transmission frequency band allows us to weight the contributions from mixed-size tissue structures, so that even structurally complex tumors (Fig 2) may be analyzed. Section 5 below describes this as an “inverse problem” where underlying structure of tissue are estimated from the echo signals generated by ultrasound interactions with the tissue.

Of course much of what we know about tissue histology is obtained from excised samples that are prepared in a manner that distorts the structural geometry. So the exact geometries of the remodeled tumor architecture is only partially known. Also the contributions to the echo signal of each cellular component at each frequency is unknown because the acoustic impedance of these structures has not yet been measured. Developing and evaluating the accuracy of a statistical description of tissue histology requires a significant amount of interdisciplinary background work to (a) identify microscopic structures that interact with sound waves, (b) measure their micro-mechanical properties, and

(c) model acoustic scattering and absorption for tumor geometries and practical acoustic fields.

### 3.2. Elasticity imaging

Another approach is related to changes in the macroscopic elastic properties of breast tissues during malignant transformation. As described above, tumors can stiffen from desmoplasia and edema more than an order of magnitude [33], which is the reason manual palpation (breast self exam) is recommended as the first line of defense for early detection. Palpation has been used successfully to detect lesions for more than two millennia despite its relatively low sensitivity for deep masses and no depth resolution. The phase sensitive nature of ultrasonic detectors allow us to measure very small tissue movements, smaller than one hundredth of a wavelength [30], with millimeter-scale depth resolution [35]. Despite the fact that sonographic spatial resolution is limited by the wavelength, the local echo phase allows us to reliably track micron-scale scatterer motion.

In elasticity imaging, the breast is scanned ultrasonically just before and after applying a small deformation force to the tissue [9]. In Fig 1(a), imagine scanning the tissue and recording the RF signals, pressing the transducer into the breast a couple of millimeters and scanning again. Comparison of the RF signals in the pre- and post-compression echo frames yields the local displacement from which strain images are computed. Strain images are an indication of the spatial variations in tissue stiffness. Any phase-sensitive imaging technique may be used: ultrasound, magnetic resonance imaging (MRI), or optical, where the resolution, sensitivity to motion and depth of penetration depend on the host modality. Many approaches to breast elasticity imaging have been proposed, and each approach provides different relative advantages [14, 21, 31, 44, 49, 59, 65]. There are also techniques for measuring the elasticity of individual cells, *in vitro* [34]. Our approach to elasticity imaging will be described in Section 6. We focus our attention on time-varying strain imaging techniques that examine the viscoelastic properties sensitive to the cellular microenvironment.

Scatterer size imaging and elasticity imaging provide complimentary but mostly independent information at different spatial scales despite the fact that both are estimated from ultrasonic RF echo frames. Imagine there is a defect in a sheet of cloth that you wish to detect. You may visually scan the cloth and look for a change in the light reflected to find the hole directly. Or you can pull on the edges of the cloth and watch how the texture of the reflected light moves over the plane as you pull. The first approach examines the microstructure where the second examines the macrostructure. Depending on the amount of contrast for each approach, one or the other or both may allow you to find the defect.

## 4. Governing Equations

Math-shy readers may want to read the words around the equations in the next section. The section is intended to briefly outline how diverse sources of mechanical disturbances in soft biological tissues can be expressed using a single mathematical expression. It gives some common ground to the many approaches to elasticity imaging as well as sonography.

Movement of an elastic tissue, which includes everything from mechanical compression to ultrasonic wave propagation, is governed by the following equation of motion [55]:

$$G\nabla^2\boldsymbol{\delta} + \left(K + \frac{G}{3}\right)\nabla(\nabla\cdot\boldsymbol{\delta}) = \rho\frac{\partial^2\boldsymbol{\delta}}{\partial t^2}, \quad (1)$$

where  $\boldsymbol{\delta}$  is the displacement vector and  $K$ ,  $G$ ,  $\rho$  are fundamental material properties of tissues. If  $\mathbf{x}_1$  is the position of a tissue scatterer at measurement time  $t_1$  and  $\mathbf{x}_2$  is the position at  $t_2$ , then  $\boldsymbol{\delta} = \mathbf{x}_2 - \mathbf{x}_1$ .  $K$  is the bulk compressibility modulus that describes how much the tissue changes volume when compressed by a known force;  $G$  is the shear modulus that describes how easily tissues change shape when stressed; and  $\rho$  is the mass density [68]. We refer to Eq (1) as a wave equation since it describes how mechanical disturbances – waves – propagate in space and time.

#### 4.1. Ultrasound waves

Under conditions where there is no rotational motion, it can be shown that  $\nabla^2\boldsymbol{\delta} = \nabla(\nabla\cdot\boldsymbol{\delta})$ , and Eq (1) reduces to the equation for compressional waves:

$$\nabla^2\boldsymbol{\delta} = \frac{1}{c^2}\frac{\partial^2\boldsymbol{\delta}}{\partial t^2}, \quad (2)$$

where  $c^2 = (K + 4G/3)/\rho$  is the speed that compressional sound waves travel. Sound speed varies between 600 m/s (lung) and 1620 m/s (lens of the eye) in soft tissues, with the average being 1540 m/s [80].

Mechanical disturbances can be described as displacement waves, as in Eq (2), or equivalently as pressure waves [28]. Thus an equation similar to (2) for plane pressure waves can be found that describes how sound energy introduced at the skin surface by a transducer flows through the body. All soft tissues are inhomogeneous in the sense that they are filled with structures that scatter a small amount of the sound wave energy (see Fig 3). These reflections are the sources of the sonographic signal. Adding the possibility of scattering to the equation, the backscattered pressure wave expressed as a function of position  $\mathbf{x} = (x, y, z)$  and temporal frequency  $f$  is

$$p_{bs}(\mathbf{x}, f, t) = \frac{k^2 P}{4\pi} \left[ \frac{\exp(-i(kx - 2\pi ft))}{x} \right] \int_{-\infty}^{\infty} d\mathbf{x}' \gamma(\mathbf{x}') \exp(-ik'x'). \quad (3)$$

Eq (3) relates the structure of the medium to the backscattered pressure waves we can measure. The integral on the right side is the complex spectrum (spatial Fourier transform) of the scatterer distribution reflecting the sound. Scatterers are spatial variations in density  $\rho$  and compressibility  $K$  that can be combined to define the acoustic impedance  $\gamma$ . The integral predicts how the size, shape, orientation and number of tissue reflectors influence the normalized backscattered amplitude.  $k^2 P/4\pi$  is an amplitude scaling factor, and the quantity in brackets shows us that a scattered wave created in tissue travels in time and space back to the receiver as a spherical wave. The backscattered pressure depends on the wavelength  $\lambda$  through the scattering wavenumber  $k' = 2k = 4\pi/\lambda$  [28]. Also  $i = \sqrt{-1}$ . Eq (3) is too simplistic for implementation, yet it guides our physical intuition and defines what is possible from tissue measurements. Section 5 provides more details about how to estimate tissue scatterer sizes from echo measurements.

#### 4.2. Static elastic deformation

Eq (1) also describes the displacement of breast tissue immediately after it is compressed in a static elasticity imaging experiment. A fundamental difference between a compressional ultrasound wave and a deformation applied during palpation is how fast the particles move during the disturbances. Particles move just 10 nm in response to a passing 10 MHz ultrasound wave with a mechanical index of 0.3 [80]. The speed of particle motion (pressure divided by acoustic impedance) at 10 MHz is roughly 540 mm/s, about 500 times faster than tissues move during palpation. Particle speed and wave speed are not the same! Particle velocity is slower than wave velocity but fast enough that the pressure wave periodically modulates the local tissue density. Consequently, we use the bulk compressibility modulus  $K$  to describe deformations from ultrasound waves. By comparison, displacements from manual palpation are too slow to affect the local density. When tissues have time to equilibrate internal forces, they change shape and not density. Consequently, the shear (shape) modulus  $G$  is the material property that describes the deformation during palpation. It is important that these two phenomena are governed by independent material properties, otherwise deformations would alter wave properties and ultrasonic echo signals could not be used to accurately track motion.

When compressed, breast tissues spring back because they are *elastic*. However, if recovery is delayed or incomplete, we say the tissue is *viscoelastic*, where the magnitude of the viscous response is proportional to the rate of deformation. All biological tissues exhibit viscoelastic behavior under common elasticity imaging conditions. Tissues are also relatively *incompressible* since the mass density changes very little during deformation. Mathematically, incompressibility implies  $\nabla \cdot \delta = 0$ . Also, if the deformation is small and slowly applied or held constant, then  $\partial^2 \delta / \partial t^2 \simeq 0$ . Therefore Eq (1) reduces to Laplace's equation  $\nabla^2 \delta = 0$ , which predicts that the displacements vary linearly with position in the body. For example, if the transducer in Fig 1a is displaced downward a distance  $\delta_0$  into the surface of the breast, along the  $x$  axis, then we would predict that the displacement along the  $x$  axis equals

$$\delta_x(x) = \bar{\epsilon}_x x + \delta_0 . \quad (4)$$

Taking two derivatives, we see Eq (4) satisfies Laplace's equation. The displacement is negative (downward) and has its largest magnitude at the skin surface,  $\delta_0$ . It decrease linearly with depth to zero at the chest wall at a rate given by the average longitudinal strain,  $\bar{\epsilon}_x = d\delta_x/dx$ . Of course, details of the boundary conditions and the geometry of mechanical inhomogeneities (like stiff tumors) perturb our simple linear equation. Nevertheless Eq (4) is used as our initial guess when reconstructing strain images from patients, as described below. Just like Eq (3), Eq (4) is too simplistic to describe real experimental details, but serves nonetheless to provide us with intuition about general tissue behavior and as an initial condition for image reconstruction.

There are several approaches to imaging viscoelastic behavior. *Dynamic elasticity imaging* methods introduce low frequency ( $<1$  KHz) shear waves into tissues [44, 49, 59, 65]. Shear waves move much slower than compressional waves and therefore they can be imaged ultrasonically or with other modalities. From the speed of the shear waves, the shear modulus of tissues is estimated almost independent of boundary conditions [22]. The problem is that tissues behave like inviscid fluids that are highly attenuating to shear

waves. We have developed *static elasticity imaging methods* for imaging viscoelastic features from a time series of strain images recorded while tissues are compressed and held [66]. The technique, its limitations, and relationship to tumor differentiation are described in Section 6.

## 5. Scatterer Size Imaging

### 5.1. Biological motivation

Optical microscopy and photomicrographs of stained histological sections represent the current gold standard for cancer diagnosis. Optical photomicrographs allow the visualization of cellular and sub-cellular structures and larger scale growth patterns of a neoplasm. In this way a definitive diagnosis of a breast lesion can often be made.

In a vast majority of cases, differentiation of benign versus malignant tumors can be made morphologically with a high degree of certainty. Four basic morphologic criteria are used to classify (or predict) malignancy of a tumor: (1) differentiation and anaplasia, (2) rate of tumor growth (3) degree of local invasion and (4) metastasis [12]. Of these criteria, optical microscopy analysis of a primary tumor describes the first three. Likewise, it is hypothesized that ultrasound scatterer size imaging of a primary tumor can also yield information related to the first three criteria.

The degree of cell differentiation is important for diagnosis. Well differentiated tumor cells have the structure and function of the tissue of origination. Conversely, anaplastic cells are undifferentiated. Typically, benign tumors are well-differentiated while malignant tumors range from well-differentiated to undifferentiated. Often times the only feature that distinguishes a benign tumor from its surroundings is the hyperplasia, or increase in cell number density. Determination of malignancy cannot always be made on the basis of cellular morphology because malignant neoplasms can be well-differentiated. However, anaplasia almost certainly means malignancy.

Morphological changes in cells related to anaplasia can be very diverse. Cells and their nuclei display variations in both shape and size (pleomorphism). Cells can be very large or very small and primitive in appearance. However, in malignant neoplasms the nuclei tend to be disproportionately large. Another feature of malignant neoplasms is the formation of giant cells that may contain one or more nuclei.

The second criteria for distinguishing malignant tumors from benign is the rate of tumor growth. In general, benign tumors grow less rapidly than do malignant tumors. The growth rate corresponds to the level of differentiation, and as a result malignant tumors (especially tumors characterized by anaplasia) grow more rapidly than benign tumors. Rapid growth of undifferentiated tumor cells is caused by an abundance of mitoses present at any one time leading to rapid proliferation. While the rate of growth is a general criteria for classifying tumors as malignant or benign, there exist benign tumors that can grow rapidly and malignant tumors that grow slowly.

The third criteria for determining malignancy is the extent of local invasion by the tumor. Nearly all benign tumors grow as solitary masses that remain localized to the site of origin. Benign tumors are most often encapsulated and do not infiltrate into surrounding tissues or vasculature. On the other hand, malignant tumors typically are accompanied by progressive invasion of the surrounding parenchyma. Exact demarcation of the

tumor margins is difficult to determine. The invasiveness of the malignant tumor can lead to metastases. The detection of metastases is the most reliable criteria for determining malignancy.

Optical microscopy can yield diagnostic information about a tumor based on the first criteria and, given a large enough sample, the third criteria. Conventional ultrasound and X-ray mammography can yield diagnostic information about the rate of growth of a tumor. We hypothesize that ultrasound spectral imaging techniques, i. e. scatterer size imaging, can further yield information regarding the first and third criteria, noninvasively.

Scatterer size imaging facilitates breast cancer diagnosis by quantifying morphological information at the cellular scale. The most common benign tumor in the female breast is a fibroadenoma. Typically fibroadenomas grow as encapsulated spherical masses. They are often freely moveable from the surrounding breast tissue. Histologically, a fibroadenoma consists of cellular and fibroblastic stroma enclosing glandular and cystic spaces. The glandular spaces (acini in Fig 1) are typically larger than  $50 \mu\text{m}$ . They are important structures for differentiating tumors that can be quantified by ultrasound scatterer size imaging techniques .

Ductal and lobular carcinomas constitute approximately 90% of all breast cancers [2]. Malignant tumors, beginning as in situ disease (DCIS and LCIS), progress to invasive cancers (IDC and ILC) as the basement membranes are breached (Fig 2). DCIS can consist of sheets of carcinoma cells and necrotic areas with microcalcifications. Cells related to DCIS appear to be monomorphic in nature unless surrounded by Paget cells (pleomorphic with abundant cytoplasm). Quantification of microcalcifications is key to making a diagnosis of DCIS and may be measurable by ultrasound scatterer size imaging. In addition, the cancer cells may have a unique, identifiable backscattering signature relative to normal cells.

As the carcinoma invades the surrounding tissue, other mechanisms take over that change the histopathological presentation. IDC is characterized by dense, scirrhous stromal tissue. Cells of IDC are highly pleomorphic (as opposed to simple DCIS) with small cells containing regular nuclei to large cells with large irregular nuclei. Often IDC infiltrates into and replaces surrounding adipose tissue. Quantification of large distributions of cell sizes may be a key to ultrasound scatterer size classification of IDC.

LCIS is characterized by a large proliferation of monomorphic epithelial cells. These cells hypertrophy with oval nuclei. Only rarely is LCIS associated with microcalcifications. The large cells may be quantifiable with scatterer size imaging yielding a unique classification signature for ultrasound. As the lobular carcinoma invades the surrounding tissue, the tumor undergoes morphological changes (Fig 2(b)). Progression of the tumor to ILC produces characteristic small cells with little pleomorphism of the nuclei. Often, ILC contains signet-ring cells. One hallmark of the ILC is the single file of cells (stacks that are often one cell wide) loosely dispersed throughout the fibrous matrix.

Each of these features may yield important ultrasound scatterer size information leading to diagnosis. The importance of understanding the underlying tissue morphology is vital to predicting and interpreting the ultrasound scatterer size images of suspicious breast lesions. In addition to suggesting possible scattering sources in a qualitative fashion, optical photomicrographs of tumors have been used to predict ultrasound backscatter signatures from tissue [43]. The motivation for using ultrasound scatterer size imaging is directly related to biological underpinnings because each type of cancer has its own

set of structural features. The next section summarizes the signal analysis for estimating size and discusses some preliminary results in animal models.

## 5.2. Scatterer size estimation

The basic approach to scatterer size estimation is simple. Estimate an echo spectrum from a small region of interest (ROI) in tissue, correct the spectrum for the instrumentation response and propagational losses, and then compare the result to a set of modeled spectral curves corresponding to different scatterer sizes. The modeled curve that best matches the data determines the average size of scatterer in the medium. The main challenge is to translate knowledge of tissue histology into accurate models of echo spectra.

RF echo signals (Fig 3) are known to contain information about the size, shape, number and relative impedance of scattering objects within the tissues [8, 27, 36]. Time-varying echo signals  $g(t)$  are coherent summations of the weak pressure waves from tissue that interact with the phase-sensitive receiving transducer surface. To estimate  $g(t)$ , we sum the pressure waves ( $p_{bs}$  from Eq (3)) over the receiver aperture area  $A$  and over frequency  $f$  after they are weighted by the acousto-electric response of the detector  $H(f)$  [27]:

$$g(t) = \int_{-\infty}^{\infty} df H(f) \int_A dA p_{bs}(\mathbf{x}, f, t) . \quad (5)$$

Scatterer size is estimated by comparing the measured backscattered power spectrum of the RF signal  $W(f)$  to modeled spectra  $W_t(f)$  where the size is known. The measured spectrum found from the squared magnitude of the short-time Fourier transform of  $g(t)$  [27]:

$$W(f) = \frac{1}{N} \frac{A(f, L)}{W_{ref}(f)} \sum_{n=1}^N |G'_n(f)|^2 , \quad (6)$$

where  $G'_n(f)$  is the Fourier transform of the time-gated RF signal of the  $n$ th scan line in the ROI,  $W_{ref}(f)$  is a reference spectrum,  $N$  is the number of gated scan lines in the ROI,  $L$  is the length of the range gate, and  $A(f, L)$  is a frequency-dependent attenuation-compensation function [51]. Increasing  $N$  reduces spectral noise but only at the cost of reduced spatial resolution for size estimates. The influence of the instrumentation parameters are minimized by normalizing  $W$  by the reference spectrum,  $W_{ref}$ . Modeled spectra,  $W_t$ , are given by [27, 36]

$$W_t(f) = C(a_e, n_z, q, L) f^4 F(f, a_e) , \quad (7)$$

where  $C$  is a constant that depends on the effective scatterer radius  $a_e$ , the average concentration of scatterer sites  $n_z$ , beam geometry factor  $q$ , and range gate length  $L$ .  $F(f, a_e)$  is the form factor that defines how scatterer size  $2a_e$  affects the frequency variations in the echo spectrum [27]. An important consideration for accurately estimating  $a_e$  is the appropriate choice of the  $F$ . Some investigators assume a Gaussian form for  $F$  that has been used to model the scattering properties of several soft tissues [29, 37, 46, 47]. Gaussian form factors represent tissue structures as continuously varying distributions of acoustic impedance fluctuations about the mean value. Numerical techniques for estimating  $2a_e$  in biological media are detailed in [53].

**Table 1.** Estimates of average scatterer size  $2a_e$  for three types of rodent tumors and corresponding healthy tissues.

Tissue type	Average Size ( $\mu\text{m}$ )
Normal	$80.2 \pm 11.2$
Fibroadenoma	$105.9 \pm 13.7$
Carcinoma	$30.0 \pm 8.9$
Sarcoma	$33.0 \pm 8.0$
Carcinoma Cell Pellet	$28.0 \pm 4.5$

### 5.3. Measurements and results

Several studies were conducted at frequencies between 5 – 25 MHz to examine the capabilities and limitations of ultrasonic scatterer size imaging. Experiments on solid tumors in rats and mice allowed us to investigate the utility of scatterer size imaging for classifying mammary tumors and describing the underlying tissue microstructure.

Three solid tumor types were studied. First, spontaneous mammary fibroadenomas in rats were examined [52]. We used a 10 MHz, single element transducer (70% bandwidth,  $f/4$ ) to estimate scatterer sizes summarized in Table 1. Initial experiments compared estimates inside the fibroadenomas with surrounding normal tissues. A statistically significant difference between average scatterer size estimates inside and outside was observed (ANOVA,  $p < 0.05$ ). Average values showed 30% increases in size for fibroadenomas. Optical photomicrographs of tumors sections, e.g., Fig 4(a), show that glandular acini have the same approximate size as the ultrasound estimates, and therefore were identified as the dominant source of scattering for the fibroadenomas. These structures are characterized by pockets of fluid surrounded by layers of epithelial cells (see Fig 1). The average size of these acini was estimated to be around  $100 \mu\text{m}$  in diameter corresponding to the ultrasonic estimates.

The second type of solid tumor was from a commercially available tumor cell line, the 4T1 MMT carcinoma for mice (ATCC, Manassas, VA). Carcinoma cells were cultured in medium and then injected subcutaneously into the fat pad of balb/c mice. Tumors were grown to a little over a centimeter in size and then examined using ultrasound scatterer size imaging. These were scanned with a 20 MHz,  $f/3$  transducer with at 75% fractional bandwidth. Results are reported in Table 1. In Fig 4(b), the individual cells themselves were identified as the most probable source of scattering in the tumors. The cells had an average nuclear diameter of  $13 \mu\text{m}$  with the total cell size being 50 to 200% larger than the nucleus. In this animal model, tumors that are allowed to grow large enough develop a necrotic core [10]. While no correlations between scatterer size imaging and necrosis in the tumors have been made to date, the possibility exists that areas of necrosis can be distinguished from regions with ample blood supply through scatterer size imaging.

The third type of solid tumor was a commercially available tumor cell line, the EHS sarcoma for mice (ATCC, Manassas, VA). Sarcoma cells were injected into mice (C57BL/6) and tumors were allowed to grow to a little over a centimeter in size before scanning. Results using the 20 MHz transducer are also shown in Table 1. Since the sarcoma scatterer size estimates were similar in size to the carcinoma estimates, it was expected that a similar type of structure would be seen in the sarcoma. However, as Fig 4(c) indicates, the structure of the sarcoma was vastly different from that of the carcinoma.

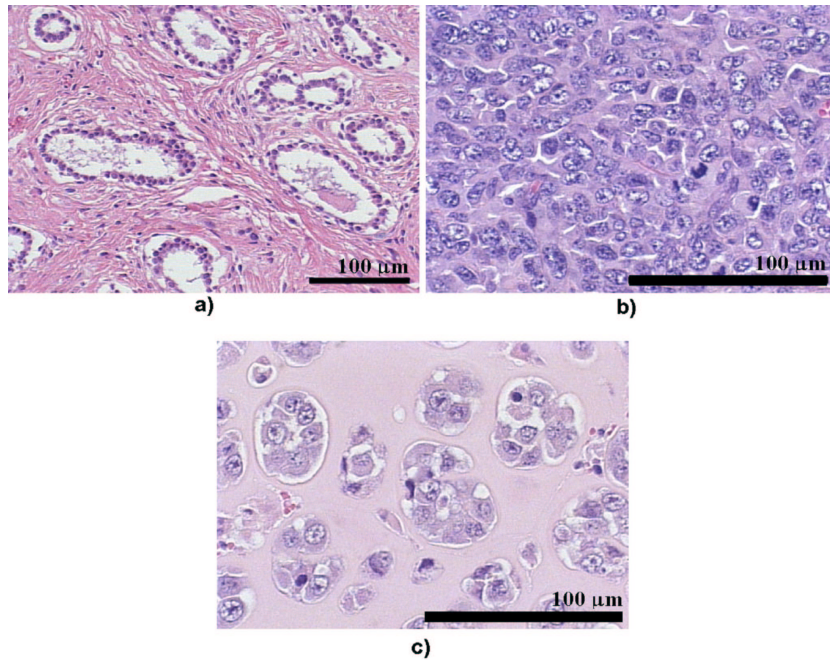


**Figure 4.** Optical photomicrographs (H & E stained) of a) rat fibroadenoma, b) mouse mammary carcinoma and c) mouse sarcoma. Reprinted with permission from Ref. [54], M.L. Oelze et al., *IEEE Trans. Med. Imaging* 23, 764 (2004) with permission from IEEE.

The sarcoma and carcinoma cells were the same size, however carcinoma cells were more uniformly distributed than the sarcoma cells. The clumps of sarcoma cells were as small as a single cell and sometimes larger than  $70 \mu\text{m}$ . They were surrounded by an ECM consisting of laminin, collagen IV, entactin and heparin proteoglycans.

Spatial maps of scatterer size estimates – parametric images – for all three types of tumors are displayed in Fig 5. The images are useful for describing how scattering structures vary in size throughout the lesion. For example, not only are the sizes larger for fibroadenomas but structures near the periphery are smaller than those near the center of the tumor.

An important consequence of culturing and transplanting cells is that the cells can be examined by themselves outside of the tumor. The 4T1 MMT carcinoma cell line is an adherent cell line; therefore, cells were grown in flasks and then placed in solution (the sarcoma cell line was not able to be used in this fashion because the cells were cultured *in vivo*). The carcinoma cells were then spun on a centrifuge for 10 minutes at 900 RPMs to form a cell pellet. The cell pellets conformed to the sides of a tube of 1 cm in diameter and the pellets had thickness typically of several millimeters. The bottom of the tube was covered with Saran Wrap (polyvinylidene chloride, SC Johnson & Sons, Racine, WI) as a scanning window to allow ultrasound to pass through and keep cellular material from escaping the tube. Comparison of ultrasonic size estimates on the pellet with those on the *in vivo* tumor showed no significant differences (Table 1). The similarity between size estimates from the tumor and from a simple pellet of cells that make up the tumor indicated that cells were the dominant source of scattering.

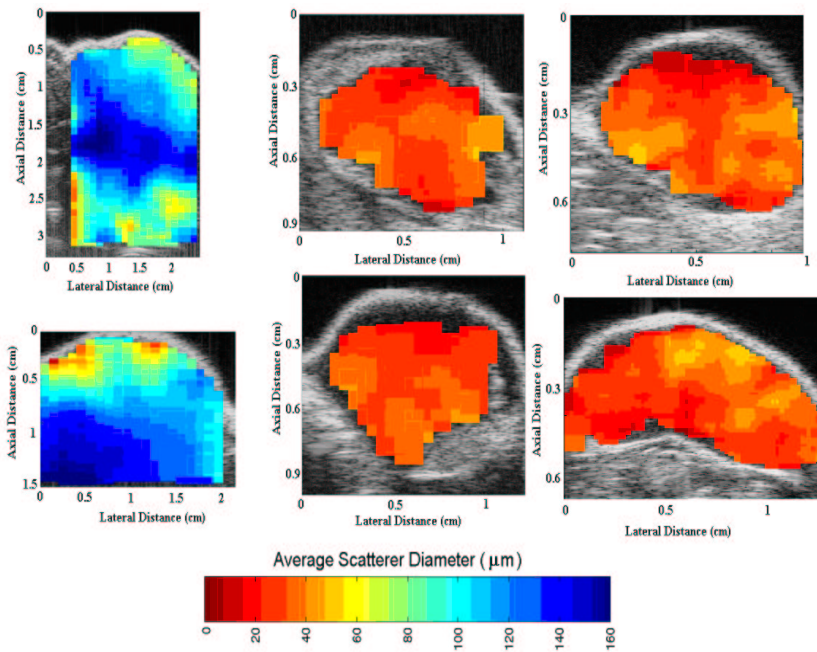


**Figure 5.** Average scatterer diameter images of rat fibroadenoma (left) mouse carcinoma (middle) and mouse sarcoma (right) tumors. Reprinted with permission from Ref. [54], M.L. Oelze et al., *IEEE Trans. Med. Imaging* 23, 764 (2004) with permission from IEEE.

The obvious differences between the carcinomas and sarcomas from the photomicrographs did not translate into significant differences in the scatterer sizes estimated using the Gaussian form factor scatterer model. We suspected that the Gaussian model was not representative of the smaller structures, and hence insufficient to separate the carcinoma from the sarcoma. The similarity between estimates indicate that cells are a dominant source of scattering in carcinoma and sarcoma. In order to see differences between the two kinds of tumors ultrasonically, several possible directions were pursued. First, it was conjectured that the larger clumping structures might be able to be picked up with much lower frequency analysis. Second, it was hypothesized that the present models for tissue scattering were not sensitive to the structural differences. More specific models would lead to a deeper understanding of the fundamental interactions of ultrasound with tissue and cellular structures. Lower frequency analysis did not yield significant differences between scatterer size estimates from carcinoma and the sarcoma tumors. Therefore, the second approach was used in an attempt to differentiate the two kinds of tumors.

The spherical Gaussian model is based on several assumptions about soft tissue scattering, i.e. the Born approximation, plane wave approximation, weakly focused sources, and no multiple scattering. These assumptions allow for soft tissue scattering to be described by a 3-D spatial autocorrelation function [29, 36]. If a distribution of the impedance in a scattering volume can be mapped out or approximated, then the normalized backscattered power spectrum can be calculated directly from this distribution [43].

Closer examination of the carcinoma tumors and cell pellets led to the initial hypothesis that the cell nucleus was the most important factor in cell scattering [54]. For

**Table 2.** Comparisons of scatterer size estimates for three different scattering models.

Tissue type	Gaussian Model		Anderson Model		New Cell Model	
	$2a_e$ ( $\mu\text{m}$ )	$\chi^2$	$2a_e$ ( $\mu\text{m}$ )	$\chi^2$	$2a_e$ ( $\mu\text{m}$ )	$\chi^2$
Sarcoma	$33.0 \pm 8.0$	11.13	$25.1 \pm 6.2$	6.9	$22.4 \pm 23.8$	9.7
Carcinoma	$30.0 \pm 8.9$	7.26	$27.7 \pm 6.6$	5.3	$16.4 \pm 20.9$	35.5

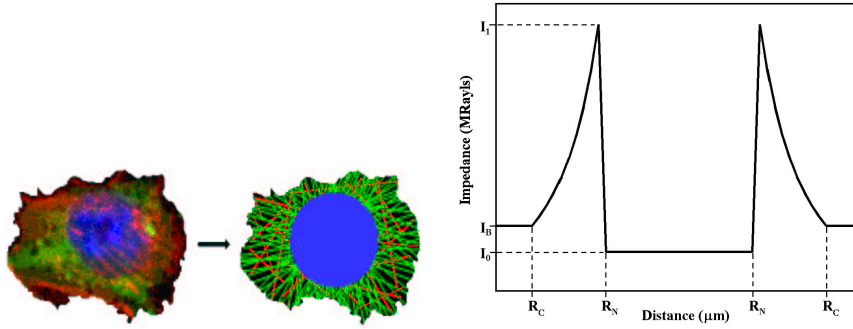


**Figure 6.** (left) Confocal microscope image of mouse carcinoma cell and subsequent cell model with actin filaments (red), microtubules (green) and nucleus (blue). (right) Acoustic model of spherical cell including effects of cytoplasm, cytoskeleton and nucleus.  $I_1$  is the impedance at the edge of the nucleus,  $I_B$  is the impedance of the background,  $I_0$  is the impedance of the nucleus,  $R_N$  and  $R_C$  are the radii of the nucleus and total cell, respectively.

carcinoma tumors and cell pellets, the fluid sphere model originally proposed by Anderson [3] seemed appropriate and was examined. We estimate scatterer sizes,  $2a_e$ , as well as the statistical metric,  $\chi^2$ , to evaluate the quality of the data fitting. Table II shows the results of the Anderson model fits to the carcinoma tumors and cell pellets compared with fits using the Gaussian model.

The Anderson model provide lower  $\chi^2$  values than the Gaussian model, implying a better fit to the spectral data. Yet the Anderson model provided no significant differences between the carcinoma and sarcoma scattering data. Furthermore, the estimated size of the scatterers obtained using the Anderson model were significantly larger than the nuclear size as observed using optical microscopy.

Closer examination of cellular structure indicated that the fluid sphere model for cell scattering was too simplistic. It should also take into account the cytoskeletal structure as well as the nuclear structure. The cytoskeleton is made up of actin filaments, microtubule network, and other organelles. The cytoskeleton is important in determining the density and compressibility of the cell body outside of the nucleus. The Anderson model assumed that the density and compressibility of the cytoplasm and cytoskeleton was constant throughout.

A new model was constructed based on the idea that the density and compressibility of the cytoskeleton played an important role in cellular scattering of ultrasound. Fig 6(left) shows a diagram of the proposed intracellular matrix structures for acoustic modeling of the cell [7, 23, 74]. The nucleus has different mechanical properties from the actin filaments and microtubules. The microtubules attach to the nucleus and fan out radially to the edges of the cell. It is conjectured that microtubules increase the average density and reduce the compressibility of the cytoplasm. Because the microtubule net-

works are bundled more densely at the surface of the nucleus and less densely at the cell edges, the impedance of the cell is modeled as a continuously increasing value from the edge of the cell to the nucleus.

The new cell model has a variable acoustic impedance as shown in Fig 6 (right). This model was used to construct a 3-D spatial autocorrelation function of the cell and therefore a new form factor model for estimating scatterer sizes from the carcinoma and sarcoma data. Table II compares these values to those of the other models. Size estimates were not much different. Also the uncertainty in estimates and  $\chi^2$  values suggest the fits to the tumor data was poor particularly for carcinoma. The poor performance of the model is most likely due to our assumptions about the acoustic impedance of the cellular organelles. As that data becomes available, the extra degrees of freedom provided by the new model will help us obtain more accurate descriptions of tissues at the cellular scale. New data also suggest that accuracy will improve as the bandwidth of transducers increases. The results suggest that scatterer size imaging could provide a noninvasive histological image of breast tumors.

No animal model can mimic all aspects of human breast cancers. Models are selected for their ability to imitate specific features of tumor growth, so the appropriateness of one animal model over another depends on the goal of the study and the tissue feature under investigation. For example, a model that exactly mimics integrin expression may be inappropriate for developing ultrasonic methods unless the organization of tumor cells and associated connective tissues also mimic human disease. There are significant differences in stromal structure between murine models and human breast cancer [75]. Unlike humans, mouse mammary stroma is primarily adipose tissue. Although the density and organization of structures are different at the macroscopic scale, the cells and associated structures are very similar. These differences do not limit the utility of mouse models for identifying the acoustic scattering sources. However rodent models are less useful for studying tissue elasticity because it is the interconnectivity among scattering structures that provides image contrast, as we now describe.

## 6. Viscoelasticity Imaging

### 6.1. Biological motivation

Mammary lobules and associated ducts in glandular tissues are key functional units and primary sites for neoplastic growth (Fig 1). As outlined in Section 2, connective tissues in glandular regions react strongly to the presence of neoplastic growth. Since connective tissues also provide most of the structural support of the tissue, it is natural to investigate whether images of viscoelastic properties could help us detect and classify lesions.

The mechanical properties of mammary glandular tissue under compression depend on the organization of the inter- and intralobular connective tissues. Both are composed of a collagenous matrix surrounded by a viscous polysaccharide ground substance [67]. This extracellular matrix constitutes most of the stromal mass. To understand how cancer affects the mechanical properties of the stroma, we examine the structure of the ECM and the fibroblasts that generate it.

It is the fibroblast cells, sparsely dispersed among the connective tissues, that form helical protein fragments from available amino acids linked by peptide bonds (see Fig

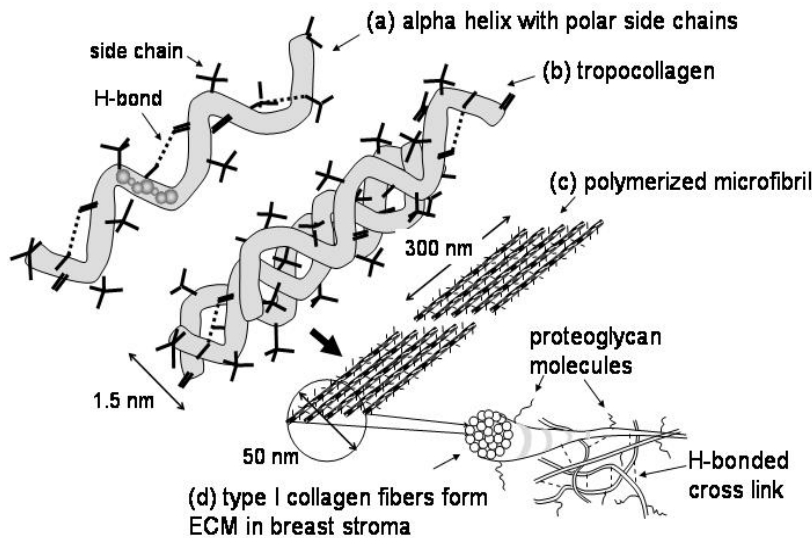


Figure 7. The molecular structure of type I collagen.

7(a)) [38]. Fragments self-assemble into triple helices with charged side-chains (Fig 7(b)) known as tropocollagen [69]. After excretion from fibroblast cells, the propeptide ends are removed and the tropocollagen polymerize into regular patterns by covalently bonding their ends to form microfibrils (Fig 7(c)) that then aggregate into cable-like bundles of type I collagen fibers (Fig 7(d)).

ECM is a random network of collagen fibers onto which hydrophilic proteoglycan molecules attach [38, 40]. Proteoglycan molecules contain sulfate groups that are dense with negative electric charges. Dense surface charges organize or “structure” the surrounding polar water molecules [15] to produce a viscous fluid – the polysaccharide gel or ground substance – that embeds the collagen matrix (Fig 8). The higher the collagen density, the more viscous is the polysaccharide gel. Cells can attach to the ECM and move along the matrix through the glycoprotein anchor points, fibronectin and laminin [11]. Normal stromal ultrastructure is constantly changing with the natural monthly growth and decline of glandular breast tissues.

Matrix fibers are interconnected at their ends and sparsely at mid points with strong covalent bonds. These generate an elastic response of the tissue to stress. Nothing we do in strain imaging changes the *covalent cross links*.

More prevalent are the much weaker and reversible *hydrogen-bonded and electrostatic cross links* found throughout the ECM. H-bonds maintain the helical shape within fibers and stabilize the matrix. Therefore they generate an elastic restoring force immediately after being stressed, but delay and dissipate some of the strain energy when the fragile bonds break and reform at a lower energy state. This is a viscoelastic response to external compression similar to the combination of spring and shock absorber on automobiles. The strength and density of inter-fiber H-bonded cross links increase with collagen

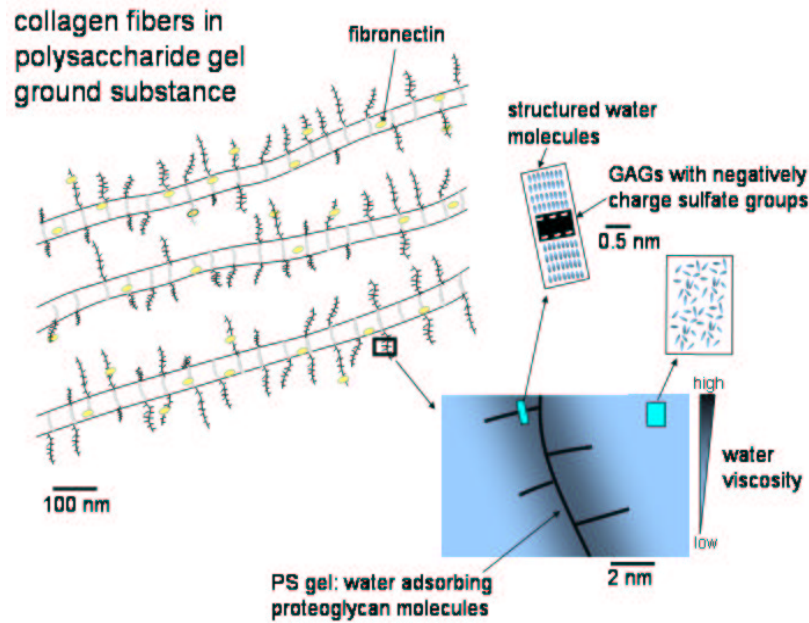
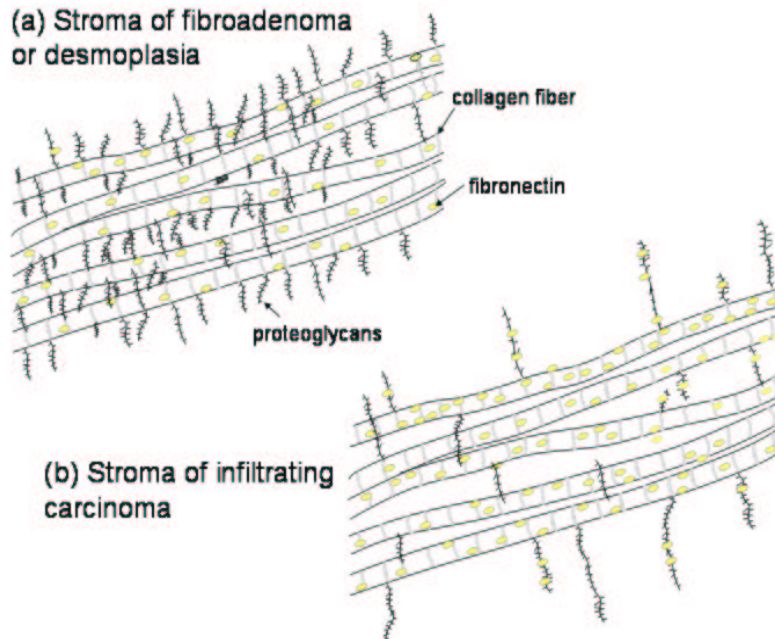


Figure 8. Ultrastructure of breast stroma.

density. Therefore it is reasonable to expect that fibrous tumors are not only stiffer than the surrounding regions but the higher cross-link density delays the full strain response for a longer time. These effects generate contrast for several viscoelastic features.

Unfortunately, as with all imaging techniques, patient diversity reduces class discriminability. It has been observed that the desmoplastic response of breast tumors varies among patients, from predominantly cellular (myofibroblast) proliferation having little added collagen to scirrhous masses with few cells [76]. Therefore elasticity imaging can be expected to reveal a range of tumor responses, from soft lesions [57] for cellular desmoplasia to very stiff lesions [33] for collagenous desmoplasia [21]; the latter are palpable while the former are not. Also, there is a reduction in relative glandular volume and the ratio of collagen to ground substance after menopause, which tend to soften breast tissues in older patients. Countering this effect is an age-dependent increase in the number of covalent bonds among collagen fibers. Depending on the balance of these effects, the viscoelastic properties of breast tissues can vary significantly with patient age. Finally, the cyclic building and eroding of normal glandular breast tissue in premenopausal women produces as much as two-fold variations in elastic moduli during the menstrual cycle [39,67]. For these reasons, spatial variation in viscoelastic properties within a breast at one point in time (image contrast) is more likely to be diagnostic than the values themselves.

Benign solid tumors, like fibroadenomas, often feature increased collagen density (Fig 9(a)). Greater fiber density reduces the inter-fiber distance fibers and increases the density of viscous ground substance. The proximity of the collagen fibers further suggests greater H-bonded cross-link density. Consequently, we expect fibroadenomas and



**Figure 9.** Changes in stromal ultrastructure for benign (a) and malignant (b) tumors.

other collagenous benign tumors to be stiffer than the surrounding tissues (palpable) and more viscous.

In infiltrating ductal carcinomas, however, the proteoglycan molecule concentration does not increase with collagen density (Fig 9(b)). Electron microscopy shows that the number of sulfated proteoglycan molecules per unit volume decrease by as much as a factor of 5 in the dense interlobular connective tissues and a factor of 14 in loose intralobular tissues [40]. The thinning of the polysaccharide gel is modified by a two-fold increase in the length of the remaining proteoglycan molecules. Thus malignant tumors can be stiffer than the surrounding tissues because of increased collagen but, unlike benign collagenous processes, the viscosity of the polysaccharide gel does not increase. Stiffness also increases as stromal fibroblasts generate large amounts of fibronectin in the tumor ECM except near the margins where fibronectin density is reduced [11]. Fibronectin density on the surface of malignant epithelial cells is also low [38]. The reduction in adhesion sites is thought to promote metastasis [62]. The patient scans in Section 6.5 show significant differences in viscoelastic properties between benign and malignant tumors that are consistent with the above molecular-scale description.

## 6.2. A physical model

Imaging techniques are best developed using simple materials with known tissue-like features – imaging phantoms. It is well known that water-based gelatin do mimic several key ultrasonic properties of breast tissues such as sound speed, dispersion, density, and frequency-dependent absorption and backscatter [41]. Like breast stroma, reconstituted gelatin is a random matrix of type I collagen fibers [77]. Unlike stroma, however, there

is no polysaccharide ground substance. Nevertheless, the elastic properties can be made reasonably tissue-like [24] despite the very different ultrastructures.

The imaging methods described below are tested using water-based gelatin gels, where mechanical properties are adjusted by varying gelatin concentration and/or adding chemical cross-linking agents. We use Type-A animal-hide gelatin (6% by volume, Fisher Chemicals, Fairlawn NJ) in a water-propanol solution with chemical cross-linkers. While basic phantom construction is detailed in [24], there are newer materials with more stable elastic features [42]. We conjecture that the collagen matrix in gelatin is representative of mammary connective-tissues regarding matrix mechanics, although the water structure near the collagen is weaker (lower viscosity) from the lack of ground substance. There is structured water due to the polar side chains on the collagen (Fig 7). For the purpose of developing imaging methods, gelatin mimics key aspects of connective breast tissues even though the viscoelastic parameters are likely to be different.

Advanced biopolymers are available for mimicking detailed features of breast tissues. Some investigators [48] study cellular developmental processes of breast cancer by culturing cells in Matrigel (BD, Franklin Lakes NJ). Matrigel is a solubilized basement membrane preparation extracted from mouse sarcoma tumors rich in ECM proteins. It has type IV collagen, laminin, and sulfated proteoglycans that provide an ECM environment for epithelial cells to study their developing morphology, biochemical function, and migration. Our studies have not yet progressed to the point where we need such a detailed phantom.

### 6.3. Mechanics of viscoelastic polymers

Much of the following section is an application of analytical solid mechanics [19, 20, 68] to polymers [17], which include mammary connective tissues. It is the physical basis for viscoelastic measurements.

The relationship between strain imaging features and connective tissue ultrastructure indicative of disease is made apparent through the constitutive equation that describes linear viscoelastic behavior of water-based polymers. The basic equation is found by applying the Boltzmann superposition principle to Hooke's law for small displacements, deformations, and deformation rates [68]. Let the stress and strain tensors be represented by  $\sigma_{ij}$  and  $\epsilon_{ij}$ , respectively. For a 3-D Hookean solid, we find the well known equation for elastic deformation [20]

$$\epsilon_{ij} = C_{ijkl}\sigma_{kl} , \quad (8)$$

where material properties of the polymer are elements of a fourth-order compliance tensor  $C_{ijkl}$ . Eq (8) describes a purely *elastic medium* where stress affects strain instantaneously. Fung [19, 20] analyzed the thermodynamics of elastic polymer deformation to show that the stresses in a deformed matrix are derived from two sources: the increase in *specific internal energy* (internal energy per mass) of the highly-structured collagen fibers (Fig 7(d)) and the decrease in specific entropy (entropy per unit mass) as random matrix fibers become spatially ordered.

Now consider the strain response of a *viscoelastic medium* to the same stress stimulus. A portion of the strain response is delayed [20]. Let the medium be initially at rest until a small (unspecified) force is applied at time  $t = t_0$ . We find that infinitesi-

mal stresses form within volume elements of the medium, and the strain responses vary in both time  $t$  and space  $\mathbf{x}$ . The stress in the volume element at  $\mathbf{x}$  is  $d\sigma_{ij}(\mathbf{x}, \tau)$ , where  $\tau = t - t_0$ . The induced strain increment is  $d\epsilon_{ij}(\mathbf{x}, t) = C_{ijkl}(\mathbf{x}, t - \tau) d\sigma_{kl}(\mathbf{x}, \tau)$  for  $\tau > 0$ . Dropping tensorial subscripts for notational simplicity, we find

$$\epsilon(\mathbf{x}, t) = \epsilon_0(\mathbf{x}) + \int_{t_0}^t d\tau C(\mathbf{x}, t - \tau) \frac{\partial \sigma}{\partial \tau}(\mathbf{x}, \tau). \quad (9)$$

$\epsilon_0(\mathbf{x})$  is the strain tensor for the instantaneous elastic response (Eq (8)) that occurs immediately after applying the load. The convolution integral on the right is the time-varying, viscoelastic response. Eq (9) tells us that strain at time  $t$  depends on the initial elastic response and a weighted sum of retarded (viscoelastic) responses.

As in many engineering problems involving linear systems, we find it easier to work in the Laplace domain than in the time domain. Adopting the notation

$$\tilde{f}(\mathbf{x}, s) = \int_0^\infty dt \exp(-st) f(\mathbf{x}, t)$$

to define the one-sided Laplace transform, Eq (9) becomes

$$\begin{aligned} \tilde{\epsilon}(\mathbf{x}, s) &= \frac{\epsilon_0(\mathbf{x})}{s} + s\tilde{C}(\mathbf{x}, s)\tilde{\sigma}(\mathbf{x}, s) \\ &= \frac{\epsilon_0(\mathbf{x})}{s} + \left[ \left( \frac{1}{9}\tilde{A}(\mathbf{x}, s) - \frac{1}{6}\tilde{U}(\mathbf{x}, s) \right) \tilde{\Sigma}(\mathbf{x}, s) + \frac{1}{2}\tilde{U}(\mathbf{x}, s) \right] \tilde{\sigma}(\mathbf{x}, s). \end{aligned} \quad (10)$$

The second form of Eq (10) is a simplification valid for isotropic media [68]. In an isotropic medium, the material properties are the same in all directions. This is an excellent assumption for the loose intra-lobular connective tissues but a weaker assumption for the dense inter-lobular connective tissues, where fibers can form patterns.  $\tilde{A}(\mathbf{x}, s)$  describes how stress on the medium element located at  $\mathbf{x}$  changes its volume, while  $\tilde{U}(\mathbf{x}, s)$  describes how stress changes its shape. Also  $\tilde{\Sigma} = (\sigma_{11} + \sigma_{22} + \sigma_{33})\delta_{ij}$ , where  $\delta_{ij}$  is the Kronecker delta.

The next step is to specify the time-varying applied stress. In static strain imaging, we apply a uniaxial ‘step-and-hold’ load to the unconfined polymer sample at  $t_0$ . (Actually we use a short-duration ramp function that approximates a step function.) This is a classic compressive *creep* experiment [68] as applied to imaging: we begin recording RF echo frames while quickly pressing the transducer into the sample a few millimeters and holding it so that the applied force remains constant over time while continuing to scan. An example of the time-varying strain (creep) curve is given in Fig 10.

The stress tensor in this experiment has just one nonzero element,  $\tilde{\sigma}_{11}(s) = \sigma_0/s$ . There are three nonzero elements of the strain tensor,  $\tilde{\epsilon}_{11}(s)$  and  $\tilde{\epsilon}_{22}(s) = \tilde{\epsilon}_{33}(s)$ . So Eq (10) gives the strain in the direction of the applied stress (and the direction of the ultrasound beam) as

$$\begin{aligned} \tilde{\epsilon}_{11}(\mathbf{x}, s) &= \frac{\epsilon_0(\mathbf{x})}{s} + \left( \frac{1}{9}\tilde{A}(\mathbf{x}, s) + \frac{1}{3}\tilde{U}(\mathbf{x}, s) \right) \tilde{\sigma}_{11}(\mathbf{x}, s) \\ &= \frac{\epsilon_0(\mathbf{x})}{s} + \tilde{D}(\mathbf{x}, s)\sigma_0/s, \end{aligned} \quad (11)$$

where  $\tilde{D}(s) \triangleq \tilde{A}(s)/9 + \tilde{U}(s)/3$  is the *viscoelastic compliance*.  $\tilde{A}$  and  $\tilde{U}$  are fundamental properties of the medium because they can be directly related to Lamé constants [68], analogous to bulk and shear moduli.  $\tilde{D}(s)$  is a derived quantity applicable to our experimental geometry, in the manner of Young's modulus. The relationship between  $\tilde{D}$  and other compliances and moduli is given in [68]. Eq (11) expresses how the one component of the strain tensor that we typically measure in static strain imaging experiments depends on material properties, via  $\tilde{D}(\mathbf{x}, s)$ , for a uniaxial compressive force applied to an unconfined polymer. Changing the experiment will result in a new equation.

We don't know anything about the viscoelastic compliance until we model Eq (11) from experiment. In this respect, viscoelastic modeling is truly an empirical science. It turns out that the response of many parenchymal tissues follows the standard (Kelvin) linear model for viscoelastic solids [20]. Adopting the Kelvin model allows us to propose physical mechanisms for the creep response that relate the constitutive equation of Eq (11) to measurements from gelatin and tissues. The Kelvin model is an  $L$ th-order discrete system [68] of the form

$$\tilde{D}(s) = \sum_{\ell=1}^L \frac{D_{\ell}}{1 + T_{\ell} s} + \left\{ \frac{1}{\eta_0 s} \right\} .$$

Braces  $\{\cdot\}$  indicate that the last term may or may not be present depending on the experimental conditions. Substituting this discrete model into Eq (11) and taking the inverse Laplace transform gives the time-varying strain imaging expression,

$$\epsilon_{11}(\mathbf{x}, t) = \epsilon_0(\mathbf{x}) + \left( \sum_{\ell=1}^L D_{\ell}(\mathbf{x})(1 - e^{-t/T_{\ell}(\mathbf{x})}) + \left\{ \frac{t}{\eta_0(\mathbf{x})} \right\} \right) \sigma_0 . \quad (12)$$

The first term on the right side of Eq (12) is the instantaneous elastic response of the medium, where most likely the stretching of covalently bonded matrix molecules contributes prominently. Immediately after applying a force, the medium behaves as an incompressible fluid. The last term (in braces) describes inelastic fluid flow; it is parameterized by the spatially-varying coefficient of viscosity  $\eta_0$ . In tissues this response could be flow in the vascular space, and in gelatin it could be nonviscinal (unstructured) interstitial water flow. In *rheodictic* media [68], the ratio  $\sigma_0/\eta_0$  is finite so the material continues to creep until it collapses. In *arrheodictic* media, as illustrated in Fig 10,  $\sigma_0/\eta_0$  is small enough that the strain plateaus and the polymer stops creeping once the viscoelastic response has relaxed. During the plateau region of the curve, the material behaves like a compressible solid. The center terms of Eq (12), represented by the summation, are viscoelastic responses. We conjecture that they are from H-bonded cross links and viscinal water flow.

An example of a second-order viscoelastic response of a hydrogel polymer during a compressive creep experiment is given in Fig 10. The amplitudes  $D_{\ell}$  and time constants of the strain retardance  $T_{\ell}$  parameterize the viscoelastic response. In *stress relaxation* experiments,  $T_{\ell}$  are *stress relaxation* time constants. However, in *creep* experiments, they define how long the strain response is delayed and thus are known as *strain retardance* time constants.

It is well known that discrete models can validate hypothesized mechanisms but cannot be used to determine the number of mechanisms (model order), as we might

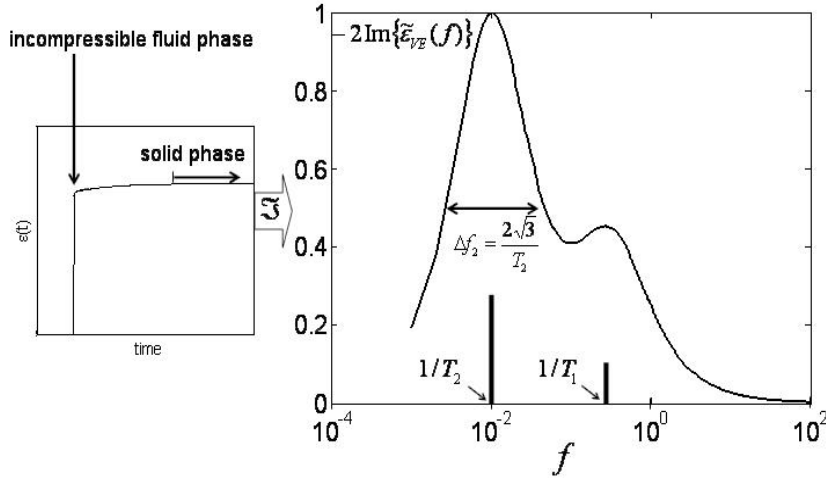


**Figure 10.** (left) A second-order viscoelastic creep curve (left) from a gelatin phantom is modeled using Eq (12) and representative parameters. Immediately after applying the force, the medium responds like an incompressible fluid. After the viscoelastic responses have decayed, the medium enters the solid phase. (right) The imaginary part of the frequency spectrum for this arrheodictic sample ( $\sigma_0/\eta_0 \simeq 0$ ) is shown. In this example  $L = 2$ ,  $D_2/D_1 = 2.5$ ,  $T_1 = 3$  s,  $T_2 = 100$  s.

hope. Fung [20] enumerates the difficulties encountered while attempting to determine the model order by fitting mathematical expressions to experimental data. While he suggests alternatives, including a continuous model of compliance, we nevertheless adopt a second- or third-order discrete model because we find it consistently fits gelatin data from our experiments. A parallel analysis in breast tissue is forthcoming.

#### 6.4. Imaging viscoelastic parameters: $\epsilon_0$ and $T_\ell$

Viscoelastic parameters are measured from a time series of strain images recorded during a step compression of the sample. The phantom experiment photographed in Fig 11 has been adapted for clinical patient scanning using freehand compression [57].

Strain images are computed from frames of recorded RF echo signals. We use a Siemens Sonoline Antares ultrasound system (Mountain View, CA) with the ultrasound research interface (URI) option that records beamformed RF frames. In a typical experiment, a VF10-5 linear array transmits broadband pulses at 10 MHz. One or two transmit focal zones are applied, and dynamic receive focusing with  $f/2$  aperture growth is used. Viewing the real-time B-mode image display and adjusting the depth-gain compensation manually to give constant echo amplitude, an operator records RF data up to 40 mm of depth at a sampling rate of 40 Msamples/s. We control the frame rate on the system's ECG triggering module from a waveform generator. Frame rates between 1 and 200 Hz can be easily selected with less than 15 ms uncertainty. Up to 0.25 GB of echo data can be recorded before it must be transferred to disk or DVD archive for off-line processing.

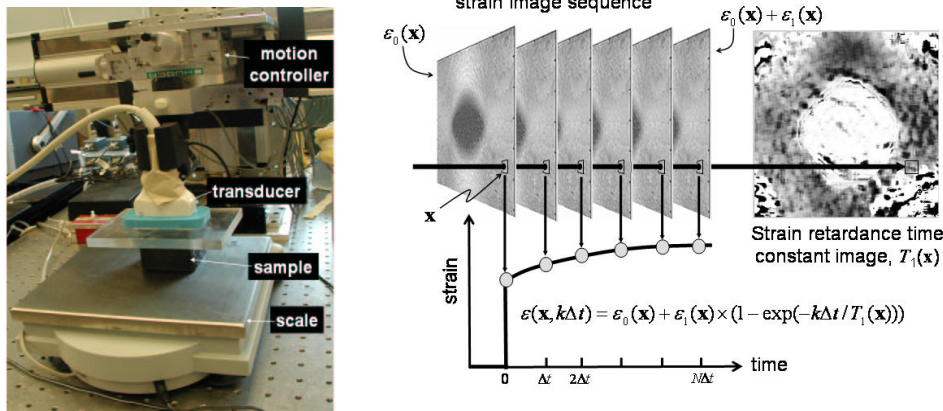


**Figure 11.** (left) Photograph of an ultrasonic viscoelastic imaging experiment using a gelatin phantom sample. (right) Method for imaging retardance time constant  $T_1$  using a time series of strain images. This arrheodictic medium is represented by a 1st-order discrete model. The central region of the phantom has three times the gelatin concentration and therefore is stiffer (dark region in strain sequence) and more viscous (longer  $T_1$ ).

Strain images are formed from correlation-based displacement estimates. Local displacements are measured from pairs of RF data frames acquired for the same region in the object at different times. Either the multi-resolution cross correlation (MRCC) algorithm [9] or the regularized optical flow algorithm [56] was applied for displacement estimation. Although there are several algorithms that might be used for local displacement estimation [22], the best choices for imaging creep curves are those with the highest sensitivity to small motion [71]. There are several overviews of ultrasonic strain imaging algorithms in the literature, e.g., [35].

With the MRCC algorithm, local displacements within the scan plane of the deformed object are found from 2-D correlation lags at different spatial scales [9]. First, the coarsest estimates of displacement are used to measure and compensate for the average displacement (see Eq (4)) applied to one frame with respect to another. The process of warping echo data in a frame to compensate for the average physical deformation is known as *global companding*.<sup>1</sup> Second, displacements measured at an intermediate-size spatial resolution are recorded and used to warp the echo fields via a local companding process. Finally, displacements are measured at the highest spatial resolution by 1-D correlation of twice companded echo frames. Interpolation provides estimates of sub-sample displacements. Components of displacement along the ultrasonic beam axis at each stage are summed and filtered by a two-sample FIR differentiator to form strain images. Axial strain pixel size is determined by parameters set at the final stage of displacement estimations. However, each stage of the estimation process and the echo impulse response of the instrumentation determine spatial resolution of the strain image [35].

<sup>1</sup>Companding is a concatenation of the words compression and expanding. It is most commonly used in the radar time delay estimation literature. In this process, displacements are estimated on a coarse spatial grid, then the pre-compression echo field is warped accordingly so it more closely matches the post-compression field [27]. The process is repeated at increasingly finer scales. Warping at one scale improves displacement estimates at a finer scale.

An RF frame acquired just prior to applying a “step” load is the reference frame to which subsequent RF frames at discrete times  $t_k = k\Delta t$  (Fig 11) are recorded and the sequence of strain images produced. Strain images are spatially registered before each pixel is fit in time to Eq (12) as shown in Fig 11. Images of  $\epsilon_0(\mathbf{x})$  (elastic strain) and  $T_\ell(\mathbf{x})$  (viscoelastic retardance times) are formed from the fits, where we set  $L = 1,2,3$  depending on the sample and the experimental conditions.

Proper sampling of the creep curves in Figs 10 and 11 is critical. This particular sampling is controlled by the RF echo frame rate. The bandwidth of the creep curve is unknown a priori since viscoelastic mechanisms for gelatin and tissues are mostly unknown. So we examine the frequency spectrum obtained from the one-sided Fourier transform of just the viscoelastic (VE) terms in Eq (12):

$$\tilde{\epsilon}_{VE}(\mathbf{x}, i\omega) = \sum_{\ell=1}^L \epsilon_\ell \left( \frac{1 - i\omega T_\ell}{1 + \omega^2 T_\ell^2} \right), \quad (13)$$

where  $\epsilon_\ell \triangleq D_\ell \sigma_0$ . The imaginary part of Eq (13) is plotted on the right side of Fig 10. For the second-order model in this example (see parameters in caption) we find spectral peaks at radial frequencies  $\omega_\ell = 2\pi T_\ell^{-1}$  given by the retardance times. The height of the peaks are  $-\epsilon_\ell/2$  and the individual peak bandwidths are  $\Delta\omega_\ell/2\pi = 2\sqrt{3}T_\ell^{-1}$  Hz (defined as full width at half maximum).

In gelatin, we often require a total acquisition time  $T_{\text{acq}} \simeq 1000$  s to observe a second-order VE processes with  $T_1 = 1-10$  s and  $T_2 = 60-150$  s. The frame rate of the ultrasound system determines the highest frequency in the spectrum of Fig 10 while  $T_{\text{acq}}$  determines the lowest frequency (= frequency resolution). In the Fig 10 example, the two VE retardance components are clearly separable. However if  $T_\ell$  values are more similar, it is unlikely they would be discriminable given that the width of each peak increases in proportion to its peak frequency. We are accumulating experience with viscoelastic measurements in gelatin to learn how to create patient images [66]. Despite the relative simplicity of cubic samples of homogeneous gelatin, we are discovering that the VE components change with fairly minor difference in experimental conditions, water context, pH, stress history, etc., while the image contrast is much less sensitive. We approached patient trials with much concern. Yet, as we show next, the early results are encouraging. Limited experience suggests that live tissues have VE components with larger amplitudes and shorter retardance times than gelatin. This is fortunate since practical acquisition times for clinical creep curves must be within a breath hold.

### 6.5. Clinical imaging

We obtained a time series of RF frames from female patients with clinically identified breast lesions that were biopsied immediately after our study. Sonograms, elastic strain images, and  $T_1$  images were obtained from one patient with two benign lesions (fibroadenomas) and a second patient with one malignancy (IDC), as shown in Fig 12. Data were acquired using the Antares system and a hand-held linear array (VF10-5) at 8 MHz. We acquired 20 frames per second over 20 seconds. Details of the RF acquisition and strain image formation algorithm are provided elsewhere [57].

As is commonly observed, each lesion is hypoechoic and appears stiffer than its surroundings. The most likely cause is edema from the lymphatic system that frequently

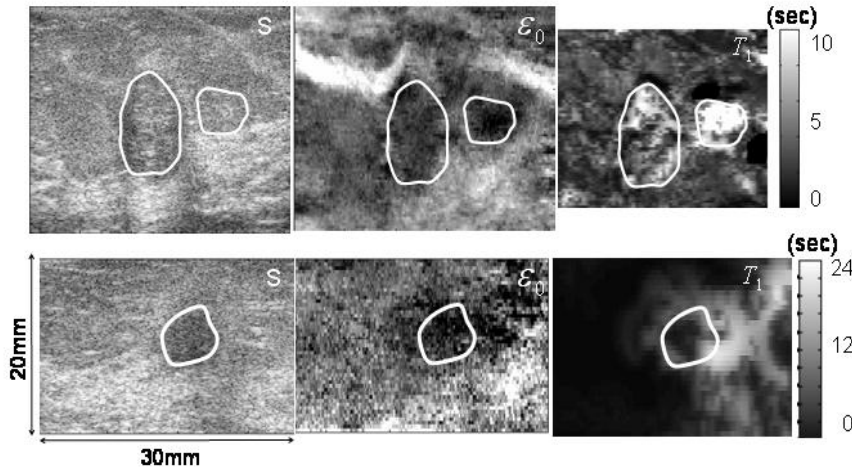


**Figure 12.** Clinical images of benign fibroadenomas (top row) and a malignant IDC (bottom row). Sonograms ( $S$ ), elastic strain images ( $\epsilon_0$ ), and retardance time constant images ( $T_1$ ) for a first-order viscoelastic model are shown. Lesions are outlined. Patient studies were acquired under an approved IRB protocol.

fails near the tumor site. In this example, the IDC tumor appears larger in the elastic strain images than in the sonogram, which is a sign of a desmoplastic response of the malignancy. Conversely, the benign lesions are approximately equal size in sonograms and strain images. Unfortunately some malignancies do not generate desmoplasia or may be of equal stiffness or softer than their surroundings [57]. Thus we increase our feature space for diagnosis by examining  $T_1$ .

Since we acquired only 20 s of data to generate our creep curve, we decided to use a first-order discrete VE model. For the benign lesions (top row of Fig 12), we clearly see a three-fold increase in  $T_1$  relative to the background. This finding is consistent with our hypothesis regarding benign lesions as outlined in Section 6.1. Despite being hypoechoic, there is an increase in the concentration of normally structured collagen. Consequently, the retardance time in the lesion increases with the greater viscosity of highly structured water: lesion  $T_1$  values are large (bright).

The malignant lesion (bottom row of Fig 12) appears to also be edematous and have increased collagen density, like the fibroadenomas, but the expected reduction in proteoglycan molecules thins the ground substance so the viscosity is roughly equal to the background. We see that  $T_1$  value is approximately 3 s, similar to background values. However, examining the region immediately surrounding the malignant lesion (an area roughly equal to the lower strain region believed to indicate desmoplasia), we see that  $T_1$  is elevated. This might indicate that the ECM within the desmoplastic reaction might have a structure similar to benign lesions. If after further study on more patients we consistently find this pattern of appearance, it is possible that  $T_1$  images may provide important new diagnostic information.

The short 20 s acquisition time used to measure the creep curve in patients is unlikely to reveal all of the viscoelastic components. If we use a 20 s acquisition time for data in Fig 10, the frequency resolution would be reduced so that the lowest frequency observed would occur at  $\omega/2\pi = 0.05$  Hz, and we would see only the low-amplitude, high-frequency peak. This was the reason we used only a first-order VE model in our early studies. Future work will include longer acquisition times to estimate and remove the  $\sigma_0 t/\eta_0$  terms and discover the bandwidth of breast tissue viscoelasticity. Nevertheless the high  $T_1$  contrast for tumor imaging is very encouraging despite the truncated acquisition of the clinical study. The appearance of the images is consistent with known changes in the molecular structure of breast stroma during disease formation.

## 7. Summary

This chapter describes ultrasonic methods for imaging mechanical properties of tissues that are useful for detection and classification of cancerous breast lesions. The methods were designed after careful consideration of the molecular biology and histology of the most prevalent disease processes. Because these techniques are new, they have not yet been subjected to the close scrutiny of comprehensive in vivo trials. Consequently we have yet to discover all the limitations that will help determine efficacy. However the preliminary results summarized here suggest that when the full diagnostic potential of ultrasonic imaging is discovered, it is likely to have a bright future for both clinical imaging and as a research tool for scientific investigation.

## Acknowledgements

The authors gratefully acknowledge colleagues and students whose work is included in this review. In particular MFI acknowledges the major contributions of Mallika Sridhar, Jie Liu, Claire Pellot-Barakat, and Karen Lindfors as well as financial support from NIH R01 CA08497. MLO wishes to acknowledge the contributions of William O'Brien, Jr. and the financial support from NIH F32 CA96419. Both authors wish to thank James F. Zachary for his helpful comments and criticisms.

## References

- [1] C.K. Abbey, A.D. Borowsky, E.T. McGoldrick, J.P. Gregg, J.E. Maglione, R.D. Cardiff and S.R. Cherry, Proc. Natl. Acad. Sci. USA **101** 11438 (2004)
- [2] American Cancer Society, Cancer Facts & Figures for 2005. [http://www.cancer.org/docroot/STT/stt\\_0.asp](http://www.cancer.org/docroot/STT/stt_0.asp).
- [3] V.C Anderson, J. Acoust. Soc. Am. **22**, 426 (1950)
- [4] J.P. Babilion, Breast Cancer Res. **3** 14, (2001)
- [5] A. Briggs, *Acoustic Microscopy*, Clarendon Press, Oxford (1991)
- [6] L.F. Brown, A.J. Guidi, S.J. Schnitt, L. Van de Water, M.L. Iruela-Arispe, T-K Yeo, K Tognazzi and H.F. Dvorak, Clinical Cancer Res. **5**, 1041 (1999)
- [7] N. Caille, O. Thoumine, Y. Tardy, and J.J. Meister, J. Biomech. **35**, 177 (2002)
- [8] J.A. Campbell and R.C. Waag, J. Acoust. Soc. Am. **74**, 393 (1983)

- [9] P. Chaturvedi, M.F. Insana and T.J. Hall, IEEE Trans. Ultrason. Ferro. Freq. Contrl. **45**, 1022 (1998)
- [10] C.P. Chikkanna-Gowda, B.J. Sheahan, M.N. Fleeton and G.J. Atkins, Gene Therapy **12**, 1253 (2005)
- [11] L. Christensen, Acta Pathologica, Microbiologica et Immunologica Scandinavica **26**, 1 (1992)
- [12] V. Kumar, A.K. Abba, and N. Fausto, *Robbins and Cotrans Pathologic Basis of Disease*, 7th ed., Elsevier-Saunders Company, Philadelphia (2005).
- [13] P. Dayton, D. Pearson, J. Clark, S. Simon, P. Schumann, R. Zutshi, T. Matsunaga, K. Ferrara, Molec. Imag. **3**, 125 (2004)
- [14] H. Dehghani, M.M. Doyley, B.W. Pogue, S. Jiang, J. Geng, and K.D. Paulsen, Phys. Med. Biol. **49**, 1131 (2004)
- [15] W. Drost-Hansen, Cell Mol. Biol. **47** 865 (2001)
- [16] B. Elenbaas, R.A. Weinberg, Exp. Cell Res. **264** 169 (2001)
- [17] J.D. Ferry, *Viscoelastic Properties of Polymers*, 3rd ed., Wiley & Sons, New York (1980)
- [18] S. Fields and F. Dunn, J. Acoust. Soc. Am. **54**, 809 (1973)
- [19] Y.C. Fung, *Foundations of Solid Mechanics*, Prentice-Hall, Engelwood Cliffs NJ (1965)
- [20] Y.C. Fung, *Biomechanics: Mechanical Properties of Living Tissues*, 2nd ed., Springer, New York (1993)
- [21] B.S. Garra, E.I. Cespedes, J. Ophir, S.R. Spratt, R.A. Zuurbier, C.M. Magnant and M.F. Penanen, Radiology **202**, 79 (1997)
- [22] J.F. Greenleaf, M. Fatemi, and M.F. Insana, in *Annual Review of Biomedical Engineering* edited M. Yarmush, Annual Reviews, Palo Alto (2003) Vol. 5, p. 57.
- [23] F. Guilak, J.R. Tedrow and R. Burgkart, Biochem. Biophys. Res. Commun. **269** 781 (2000)
- [24] T.J. Hall, M. Bilgen, M.F. Insana and T. Krouskop, IEEE Trans. Ultrason. Ferro. Freq. Contrl. **UFFC-44** (1997) 1355-1365.
- [25] A.R. Howlett and M.J. Bissell, Epithelial Cell Biol. **2**, 79 (1993)
- [26] D.E. Ingber, Differentiation **70**, 547 (2002)
- [27] M.F. Insana, R.F. Wagner, D.G. Brown and T.J. Hall, J. Acoust. Soc. Am. **87** 179 (1990)
- [28] M.F. Insana and D.G. Brown, in *Ultrasonic Scattering in Biological Tissues* edited K.K. Shung and G.A. Thieme, CRC Press, Boca Raton (1993) p. 75.
- [29] M.F. Insana, J. Acoust. Soc. Am. **97**, 649 (1995)
- [30] M.F. Insana, L.T. Cook, M. Bilgen, P. Chaturvedi and Y. Zhu, J. Acoust. Soc. Am. **107**, 1421 (2000)
- [31] M.F. Insana, C. Pellot-Barakat, M. Sridhar and K.K. Lindfors, J. Mammary Gland Biol. Neoplasia **9**, 393 (2004)
- [32] R.K. Jain, Nat. Med. **9**, 685(2003)
- [33] T.A. Krouskop, T.M. Wheeler, F. Kallel, B.S. Garra and T. Hall, Ultrason. Imaging **20**, 260 (1998)
- [34] B. Lincoln, H.M. Erickson, S. Schinking, F. Wottawah, D. Mitchell, S. Ulvick, C. Bilby and J. Guck, Cytometry A **59**, 203 (2004)
- [35] J. Liu, C.K. Abbey and M.F. Insana, IEEE Trans. Ultrason. Ferroelectr. Freq. Control **51**, 716 (2004)
- [36] F.L. Lizzi, M. Greenebaum, E.J. Feleppa, M. Elbaum and D.J. Coleman, J. Acoust. Soc. Am. **73**, 1366 (1983)
- [37] F.L. Lizzi, M. Ostromogilsky, E.J. Feleppa, M.C. Rorke and M.M. Yaremko, IEEE Trans. Ultrason. Ferroelect. Freq. Cont. **33**, 319 (1987)
- [38] H. Lodish, A. Berk, P. Matsudaira, C.A. Kaiser, M. Krieger, M.P. Scott, S.L. Zipursky and J. Darnell, *Molecular Cell Biology*, 5th ed., W.H. Freeman and Co., New York (2004)
- [39] J. Lorenzen, R. Sinkus, M. Biesterfeldt and G. Adam, Invest. Radiol. **38**, 236 (2003)
- [40] G.A. Losa and M. Alini, Int. J. Cancer **54**, 552 (1993)
- [41] E.L. Madsen, J.A. Zagzebski and G.R. Frank, Ultrasound Med. Biol. **8**, 381 (1982)

- [42] E.L. Madsen, G.R. Frank, T.A. Krouskop, T. Varghese, F. Kallel and J. Ophir, *Ultrason. Imaging* **25**, 17 (2003)
- [43] J. Mamou, M.L. Oelze, W.D. O'Brien and J.F. Zachary, *J. Acoust. Soc. Am.* **117**, 413 (2005)
- [44] A.L. McKnight, J.L. Kugel, P.J. Rossman, A. Manduca, L.C. Hartmann and R.L. Ehman, *Am. J. Roentgenol.* **178**, 1411 (2002)
- [45] K.D. Miller, C.J. Sweeney and G.W. Sledge Jr., *Ann Oncol.* **14**, 20 (2003)
- [46] D.K. Nassiri and C.R. Hill, *J. Acoust. Soc. Am.* **87**, 2048 (1986)
- [47] D. Nicholas, *Ultrasound Med. Biol.* **8**, 17 (1982)
- [48] C. Niemann, V. Brinkmann, E. Spitzer, G. Hartmann, M. Sachs, H. Naundorf and W. Birchmeier, *J. Cell Biol.* **143**, 533 (1998)
- [49] K. Nightingale, S. McAleavey and G. Trahey, *Ultrasound Med. Biol.* **29**, 1715 (2003)
- [50] V. Ntziachristos and B. Chance, *Breast Cancer Res.* **3**, 41 (2001)
- [51] M.L. Oelze and W.D. O'Brien, Jr., *J. Acoust. Soc. Am.* **111**, 2308 (2002)
- [52] M.L. Oelze, J.F. Zachary and W.D. O'Brien, Jr., *J. Ultrasound Med.* **21**, 1201 (2002)
- [53] M.L. Oelze, J.F. Zachary and W.D. O'Brien Jr., *J. Acoust. Soc. Am.* **112**, 1202 (2002)
- [54] M.L. Oelze, W.D. O'Brien Jr, J.P. Blue and J.F. Zachary, *IEEE Trans. Med. Imaging* **23**, 764 (2004)
- [55] K.J. Parker, L.S. Taylor and S. Gracewski, *J. Acoust. Soc. Am.* **117**, 2705 (2005)
- [56] C. Pellot-Barakat, F. Frouin, M.F. Insana and A. Herment, *IEEE Trans. Med. Imaging* **23**, 153 (2004)
- [57] C. Pellot-Barakat, M. Sridhar, K.K. Lindfors and M.F. Insana, *Current Med. Imaging Rev.* **2**, (2006) (in press).
- [58] O.W. Petersen, H.L. Nielsen, T. Gudjonsson, R. Villadsen, L. Ronnov-Jessen and M.J. Bissell, *Breast Cancer Res.* **3**, 213 (2001)
- [59] D.B. Plewes, J. Bishop, A. Samani and J. Sciarretta, *Phys. Med. Biol.* **45**, 1591 (2000)
- [60] F.D. Rollo, *Radiol Manage.* **25**, 28 (2003)
- [61] L. Ronnov-Jessen, O.W. Petersen and M.J. Bissell, *Physiol Rev.* **76**, 69 (1996)
- [62] E. Ruoslahti and E. Engvall, *Biochim. Biophys. Acta* **631**, 350 (1980)
- [63] W. Schurch, T.A. Seemayer and R. Lagace, *Virchows Arch.* **391**, 125 (1981)
- [64] M.D. Sherar, M.B. Noss and F.S. Foster, *Nature* **330**, 493 (1987)
- [65] R. Sinkus, M. Tanter, T. Xydeas, S. Catheline, J. Bercoff and M. Fink, *Magn. Reson. Imaging* **23**, 159 (2005)
- [66] M. Sridhar and M.F. Insana, in *Lecture Notes in Computer Science Series* editors G. Christensen and M. Sonka, (2005) Vol. 3565, p. 516.
- [67] M. Stoeckelhuber, P. Stumpf, E.A. Hoefter and U. Welsch, *Histochem. Cell. Biol.* **118**, 221 (2002)
- [68] N.W. Tschoegl, *Phenomenological Theory of Linear Viscoelastic Behavior: An Introduction*, Springer, New York (1989)
- [69] M. van der Rest and R. Garrone, *FASEB J.* **5**, 2814 (1991)
- [70] T. Velling, J. Risteli, K. Wennerberg, D.F. Mosher and S. Johansson, *J. Biol. Chem.* **277**, 37377 (2002)
- [71] F. Viola and W.F. Walker, *IEEE Trans. Ultrason. Ferroelectr. Freq. Control* **52**, 80 (2005)
- [72] R. Vracko, *Am J Pathol.* **77**, 314 (1974)
- [73] R.F. Wagner, M.F. Insana and D.G. Brown, *J. Opt. Soc. Am. A* **4**, 910 (1987)
- [74] O. Wagner, J. Zinke, P. Dancker, W. Grill and J. Bereiter-Hahn, *Biophysic. J.* **76**, 2784 (1999)
- [75] K.U. Wagner, *Breast Cancer Res.* **6**, 31 (2004)
- [76] R.A. Walker, *Breast Cancer Res.* **3**, 143 (2001)
- [77] A.G. Ward, *Br. J. Appl. Physics* **5**, 85 (1954)
- [78] B. Weigelt, J.L. Peterse and L.J. van't Veer, *Nature Reviews Cancer* **5**, 591 (2005)
- [79] R. Weissleder and U. Mahmood, *Radiology* **219**, 316 (2001)
- [80] J.A. Zagzebski, *Essentials of Ultrasound Physics* Mosby, St. Louis (1996)